Available online at www.sciencedirect.com

ScienceDirect

Advances in Space Research 71 (2023) 1363–1376

ADVANCES IN SPACE RESEARCH
(a COSPAR publication)

www.elsevier.com/locate/asr

A method of real-time long-baseline time transfer based on the PPP-RTK

Kan Wang [a,b,*], Baoqi Sun [a,b], Weijin Qin [a,b], Xiaolong Mi [c], Ahmed El-Mowafy [c]
Xuhai Yang [a,b]

[a] *National Time Service Center, Chinese Academy of Sciences, Xi'an, China*
[b] *University of Chinese Academy of Sciences, Beijing, China*
[c] *School of Earth and Planetary Sciences, Curtin University, Perth, Australia*

Received 20 August 2022; received in revised form 20 October 2022; accepted 26 October 2022
Available online 1 November 2022

Abstract

Long-baseline time transfer can nowadays reach rather high frequency stability based on post-processed batch least-squares adjustment using the Precise Point Positioning (PPP) or Integer-PPP (IPPP) methods. For real-time PPP users, time transfer results are degraded due to the filter-based processing mode, and the degraded accuracy of the real-time satellite orbits and clocks compared to the final ones. The Real-Time Kinematic (RTK) time transfer can significantly reduce the satellite-related errors, but has limits on the baseline length similar to the RTK positioning. Also, the delivery of raw observations instead of State-Space Representation (SSR) products could result in pressure on data transfer and difficulties related to latency and prediction. In this study, the PPP-RTK technique, which combines the advantages of the PPP and the RTK methods, is tested for real-time long-baseline time transfer. As an alternative approach to the above two methods, it allows for the time transfer of long baselines, while not relying on external high-sampling and high-precision satellite clocks. By delivering the satellite clocks and satellite phase biases produced within the PPP-RTK regional network, time differences can be estimated between users and the reference network station, with which stable time transfer between users separated by long baselines can be realized. Using dual-frequency GPS and Galileo data, the PPP-RTK time transfer is tested using approximately a thousand-kilometer-scale network in Europe. The time transfer results between two hydrogen masers, i.e., those on the 884 km baseline BRUX-ONSA and the 920 km baseline WTZR-ONSA, are computed. At an averaging time of 10^5 s, Modified Allan Deviation (MDEV) at the level of sub-10^{-15} to 10^{-15} can be reached when processing the user coordinates in the station fixed, static, or kinematic modes. The median clock residuals can converge to 1 ns and 0.3 ns within 2 min and 15 min, respectively, in the kinematic mode, while in the static and fixed modes the convergence times are shorter. With the augmentation of 150 Low Earth Orbit (LEO) satellites having simulated observations, the clock residuals can converge to 1 ns and 0.3 ns within 30 s and 3.5 min, respectively, for all the three estimation modes.

Keywords: Time Transfer; PPP-RTK; Long-Baseline; Real-Time; Timing

1. Introduction

The Global Navigation Satellite Systems (GNSSs) have been used for the Positioning, Navigation and Timing (PNT) services over the past decades. Benefiting from the high precision of the final GNSS satellite orbital and clock products provided by different institutions,

---

[*] Corresponding author at: National Time Service Center, Chinese Academy of Sciences, Xi'an, China; University of Chinese Academy of Sciences, Beijing, China.
E-mail address: wangkan@ntsc.ac.cn (K. Wang).

https://doi.org/10.1016/j.asr.2022.10.062
0273-1177/© 2022 COSPAR. Published by Elsevier B.V.

e.g., the International GNSS Service (IGS) (Noll 2010), the Precise Point Positioning (PPP) method has achieved very good frequency stability in time transfer. The Integer-PPP (IPPP), having the integer ambiguities resolved with the help of satellite phase biases, further improves the long-term stabilities of the time transfer to an excellent level (Petit et al. 2015), reaching the sub-10^{-16} level at an averaging time of one week (Petit et al. 2017; Petit 2021).

Nowadays, the need for time transfer is extended to real-time areas, e.g., fast capture of clock anomalies and unmanned simultaneous automatic seeding. To fulfill the needs of real-time users, the Real-Time (RT) PPP and IPPP methods were also investigated for time transfer, applying high-precision real-time satellite orbits and clocks within an extended Kalman filter (Lyu et al. 2019; Qin et al. 2021). The RT PPP/IPPP time transfer has a degraded performance compared to the post-processed mode. This is, on the one side, caused by the decreased precision of the real-time GNSS satellite orbits and clocks, and on the other side, related to the filter-based processing mode compared to the batch least-squares adjustment used for the post-processing.

In contrast to differencing two independently estimated receiver clock parameters, the receiver clock difference can be directly estimated within a baseline. The idea of the Real-Time Kinematic (RTK) time transfer was investigated in various studies (Feng and Li, 2010; Sun et al. 2021; Tu et al. 2021; Xue et al. 2021). Single-differenced observations were used to directly estimate the between-receiver clock biases, with optionally fixed ambiguities at the double-difference level. The high precision requirement on the satellite orbits is relieved in such a case. The satellite clocks are eliminated by differencing, with the day boundary problems avoided at the same time. However, similar to the RTK positioning, the performance of the RTK time transfer is limited by the baseline length due to the influences of the atmospheric residuals. The method thus works better for short baselines. Also, to be mentioned, is that the differencing of the RTK time transfer is performed on the observation level, which requires the transfer of raw observations instead of the satellite-related products in the State-Space Representation (SSR). This could lead to pressure on the data transfer. The prediction also becomes difficult in case of data loss or latency.

Taken into consideration all the advantages and limitations of the methods mentioned above, in this contribution, a new approach for long-baseline real-time time transfer is proposed based on the PPP-RTK technique. As first introduced by Wübbena et al. (2005), the PPP-RTK method combines the advantages of the PPP and the RTK, i.e., enabling a fast convergence to high precision while guaranteeing a certain level of independence of nearby infrastructure for the user (Teunissen et al. 2010). In this study, the proposed PPP-RTK time transfer method is based on the Undifferenced and Uncombined (UDUC) model. The UDUC model is advantageous in the sense that it can be strengthened by applying spatial or temporal constraints to the parameters that otherwise could be eliminated through differencing or combination. The model is also free to be extended to an arbitrary number of frequencies (Odijk et al. 2015). Compared to the PPP (or IPPP) methods, it does not rely on high-sampling and high-precision satellite clocks from external sources, but produces the satellite clocks and phase biases within its own regional network processing. It estimates the Zenith Tropospheric Delays (ZTDs) and ionospheric delays within the observation model, so that it is not limited to short baselines when applying the so-called ionosphere-float model (Odijk et al. 2015). The network delivers the users with satellite-related products instead of raw observations, which eases data transfer and the need for short-term predictions. By adding a time link in the hardware biases, the estimable receiver clock could formally get rid of the time-varying receiver code bias (will be addressed in Section 2). This could be beneficial to users when the variation of the receiver hardware biases strongly influences the time-transfer results.

In this contribution, the frequency instability of the long-baseline time transfer is investigated in the real-time mode using a large-scale regional network tracking real GPS and Galileo signals. The time transfer results are studied for the cases in which the user coordinates are known and considered fixed, or estimated in static and kinematic modes. A method to combine the receiver clock differences processed based on multi-constellation signals is introduced. The frequency instability of the combined PPP-RTK between-receiver clock is analyzed for two long links of 800–1000 km connecting stations equipped with Hydrogen Masers (H-Masers). In addition to this, the convergence time of the clock residuals is another issue of concern for real-time users. In this study, the convergence time is not only discussed for different estimation modes using real GNSS signals, the investigation is extended for possible low Earth orbit (LEO) augmentation in the future. In recent years, LEO satellites have been frequently discussed for augmenting the PNT service due to their numerous advantages with their lower orbital heights (Reid et al. 2018; Wang et al. 2022a). With their higher speed and more rapid geometry change for ground users, the convergence time is found to be significantly shortened for the PPP (Li et al. 2019) and the PPP-RTK positioning (Wang et al. 2022a). In this contribution, with the registered configuration of the navigation-oriented LEO satellite constellation, CentiSpace, of 150 satellites (Yang 2019; Wang et al. 2022a), the benefits of the LEO augmentation are discussed for the convergence time of the PPP-RTK timing.

The paper starts with a short introduction of the UDUC PPP-RTK model of the network and the user parts. This is followed by the description of the measurement setup. The section concerning testing results is split into three parts, i.e., i) the multi-constellation combined clocks; ii) the frequency instability; and iii) the convergence time with an extension of the LEO augmentation. Conclusions are given at the end of the paper.

2. Processing strategy

The UDUC model does not attempt to eliminate unknown parameters by differencing or combination, but keeps them all in the observation model. To avoid the singularities among the parameters, the S-system theory (Baara 1981; Teunissen 1985) is used, with a set of S-basis parameters not estimated and new estimable parameters reformed. According to the temporal and spatial models applied to the parameters, the formulation of the parameters could vary under different conditions (Odijk et al. 2015). In this contribution, the parameter formulation is discussed for the ionosphere-float model with all the satellite and receiver hardware biases considered linked in time. The processing models for the network and user parts are introduced in the following two sub-sections. The forms of the estimated user receiver clocks and their differences will be discussed in Section 2.2.

2.1. Network processing

With corrections like the hydrostatic tropospheric delay, the receiver and satellite antenna Phase Center Offsets (PCOs) and Phase Center Variations (PCVs), their antenna sensor offsets, the phase windups, the relativistic effects, and the solid Earth tides considered in the Observed-minus-Computed (O—C) terms, the phase ($\Delta\varphi^s_{r,j}$) and code ($\Delta p^s_{r,j}$) O—C terms can be formulated as follows, using the parameters in their original forms:

$$\begin{aligned} \mathrm{E}\left(\Delta\varphi^s_{r,j}\right) &= g^s_r\Delta\tau_r + dt_r - dt^s - \mu_j\iota^s_r + \delta_{r,j,g} - \delta^s_{,j} \\ &\quad + \lambda_j N^s_{r,j} \end{aligned} \tag{1}$$

$$\mathrm{E}\left(\Delta p^s_{r,j}\right) = g^s_r\Delta\tau_r + dt_r - dt^s + \mu_j\iota^s_r + d_{r,j,g} - d^s_{,j} \tag{2}$$

where the subscripts r and g denote receiver r and constellation g, respectively. The satellite number s is counted among all the used constellations, and j refers to the j-th frequency used for the relevant constellation. $\mathrm{E}(\cdot)$ denotes the expectation of the contents contained in $(\cdot)$. The wet part of the ZTD is mapped with the Ifadis mapping function g^s_r (Ifadis 1986) into the Line-Of-Sight (LOS) direction. The receiver and satellite clock biases are denoted with dt_r and dt^s expressed as distances, respectively. The L1 ionospheric delay ι^s_r is multiplied with the dispersive factor $\mu_j = f_1^2/f_j^2$ for frequency f_j. The receiver hardware biases distinguish between phase $\left(\delta_{r,j,g}\right)$ and code $\left(d_{r,j,g}\right)$ measurements. The same also applies to the satellite hardware biases for phase ($\delta^s_{,j}$) and code ($d^s_{,j}$). The integer ambiguity $N^s_{r,j}$ is multiplied with the wavelength λ_j on the corresponding frequency. The network station coordinates are fixed to their known ground truths post-processed in daily batch least-squares adjustment.

As mentioned before, the parameters in Eqs. (1) and (2) need to be reformed to avoid singularities. The re-formed parameters are denoted with a tilde sign above the symbols as follows, except for the ZTD $\Delta\tau_r$ that keeps its original form, such that:

$$\begin{aligned} \mathrm{E}\left(\Delta\varphi^s_{r,j}\right) &= g^s_r\Delta\tau_r + \widetilde{dt}_{r,g} - \widetilde{dt}^s - \mu_j\widetilde{\iota}^s_r + \widetilde{\delta}_{r,j,g} - \widetilde{\delta}^s_{,j} \\ &\quad + \lambda_j\widetilde{N}^s_{r,j} \end{aligned} \tag{3}$$

$$\mathrm{E}\left(\Delta p^s_{r,j}\right) = g^s_r\Delta\tau_r + \widetilde{dt}_{r,g} - \widetilde{dt}^s + \mu_j\widetilde{\iota}^s_r + \widetilde{d}_{r,j,g} - \widetilde{d}^s_{,j} \tag{4}$$

With all the hardware biases assumed to be linked in time, the S-basis parameters are selected as $dt_1(t_i)$, $d_{1,j,g}(t_1)$, $\delta_{1,j,g}(t_1)$, $N^s_{1,j}(t_i)$, $N^1_{r,j,g}(t_i)$, $d_{r\neq1,j=1,2,g}(t_1)$, $d^s_{,j=1,2}(t_1)$, where the subscript 1 and superscript 1 denote the reference station and satellite (in the corresponding constellation g), respectively. t_i denotes the time of the i-th processing epoch.

In Eqs. (3) and (4), the estimable receiver clock bias $\widetilde{dt}_{r,g}$ varies for different constellations g, as the between-receiver ionosphere-free (IF) code bias $d_{1r,\mathrm{IF},g}$ at the first epoch t_1 is lumped into it at epoch i:

$$\widetilde{dt}_{r,g}(t_i) = dt_{1r}(t_i) + d_{1r,\mathrm{IF},g}(t_1) \tag{5}$$

where $(\cdot)_{,\mathrm{IF}} = \left(\mu_2(\cdot)_{,1} - \mu_1(\cdot)_{,2}\right)/(\mu_2 - \mu_1)$. The forms of other estimable parameters are formulated as follows (Odijk et al. 2015; Wang et al. 2021):

$$\widetilde{dt}^s(t_i) = dt^s(t_i) + d^s_{,\mathrm{IF}}(t_1) - dt_1(t_i) - d_{1,\mathrm{IF},g}(t_1) \tag{6}$$

$$\widetilde{\iota}^s_r(t_i) = \iota^s_r(t_i) + d_{r,\mathrm{GF},g}(t_1) - d^s_{,\mathrm{GF}}(t_1) \tag{7}$$

$$\begin{aligned} \widetilde{\delta}_{r,j,g}(t_i) &= \delta_{r,j,g}(t_i) - \delta_{1,j,g}(t_1) + \mu_j d_{1r,\mathrm{GF},g}(t_1) \\ &\quad - d_{1r,\mathrm{IF},g}(t_1) + \lambda_j N^1_{1r,j,g}(t_i) \end{aligned} \tag{8}$$

$$\begin{aligned} \widetilde{\delta}^s_{,j}(t_i) &= \delta^s_{,j}(t_i) + \mu_j\left(d^s_{,\mathrm{GF}}(t_1) - d_{1,\mathrm{GF},g}(t_1)\right) - d^s_{,\mathrm{IF}}(t_1) \\ &\quad + d_{1,\mathrm{IF},g}(t_1) - \delta_{1,j,g}(t_1) - \lambda_j N^s_{1,j}(t_i) \end{aligned} \tag{9}$$

$$\begin{aligned} \widetilde{d}_{r,j,g}(t_i) &= d_{r,j,g}(t_i) - d_{1,j,g}(t_1) - d_{1r,\mathrm{IF},g}(t_1) \\ &\quad - \mu_j d_{1r,\mathrm{GF},g}(t_1) \end{aligned} \tag{10}$$

$$\begin{aligned} \widetilde{d}^s_{,j}(t_i) &= d^s_{,j}(t_i) - d^s_{,\mathrm{IF}}(t_1) - \mu_j d^s_{,\mathrm{GF}}(t_1) - d_{1,j,g}(t_1) \\ &\quad + d_{1,\mathrm{IF},g}(t_1) + \mu_j d_{1,\mathrm{GF},g}(t_1) \end{aligned} \tag{11}$$

$$\widetilde{N}^s_{r,j}(t_i) = N^s_{1r,j}(t_i) - N^1_{1r,j,g}(t_i) \tag{12}$$

$$(\cdot)_{,\mathrm{GF}} = \left((\cdot)_{,2} - (\cdot)_{,1}\right)/(\mu_2 - \mu_1)$$

The hardware biases and the ZTDs are separately linked in time with random-walk processes. The spectral density parameters are set to 0.0001 $\mathrm{m}/\sqrt{s}$ for the ZTDs ($\Delta\tau_r$), the satellite phase ($\widetilde{\delta}^s_{,j}$) and code biases ($\widetilde{d}^s_{,j}$). It is set to 0.001 $\mathrm{m}/\sqrt{s}$ for the receiver phase ($\widetilde{\delta}_{r,j,g}$) and code biases ($\widetilde{d}_{r,j,g}$). The ambiguities $\widetilde{N}^s_{r,j}$ are constrained as constants before a cycle slip is detected. The parameters are updated every epoch with the sequential least-squares adjustment, considering the time links mentioned above. The elevation-dependent weighting function $\sin^2(\theta_e)$ is applied for both the phase and code observations, with θ_e denoting the elevation angle. The elevation cut-off angle is set to 10 degrees. The zenith-referenced standard deviations for phase and code are set to 0.003 and 0.3 m, respectively.

With the ambiguity-float network solutions calculated, it is possible to resolve the double-differenced ambiguities $\widetilde{N}^{s}_{r,j}$ to integers. The Least-Squares Ambiguity Decorrelation Adjustment (LAMBDA) method (Teunissen 1993; 1995) is an efficient method for ambiguity resolution, which reforms the de-correlated ambiguities before searching for the integers. In this contribution, the Partial Ambiguity Resolution (PAR) approach (Nardo et al. 2016) is applied with the LAMBDA method. It allows a sub-set of the ambiguities to be first resolved when the full set cannot reach the pre-defined Ambiguity Success Rate (ASR), here defined as 99.99 % for the network processing. To validate the resolved ambiguities, a ratio test is performed with the threshold set to three (Leick 2004; Teunissen and Verhagen 2004), such that:

$$\frac{R_1}{R_2} < 3 \tag{13}$$

where R_1 and R_2 are the weighted squared norms of the ambiguity residuals for the best and the second-best sets of ambiguity candidates, respectively. In case the ratio test does not pass, the de-correlated ambiguity is kicked out, one by one, until the ratio test passes.

2.2. User processing

On the user side, the estimable parameters are transformed consistently with the network part. The phase ($\Delta\varphi^{s}_{u,j}$) and code ($\Delta p^{s}_{u,j}$) O—C terms can be expressed as:

$$\begin{aligned}\mathrm{E}\left(\Delta\varphi^{s}_{u,j} + \widehat{\widetilde{dt}}^{s} + \widehat{\widetilde{\delta}}^{s}_{,j}\right) = {} & \left(G^{s}_{u}\right)^{\mathrm{T}}\Delta x_u + g^{s}_{u}\Delta\tau_u + d\widetilde{t}_{u,g} \\ & - \mu_j \widetilde{\iota}^{s}_{u} + \widetilde{\delta}_{u,j,g} + \lambda_j \widetilde{N}^{s}_{u,j}\end{aligned} \tag{14}$$

$$\begin{aligned}\mathrm{E}\left(\Delta p^{s}_{u,j} + \widehat{\widetilde{dt}}^{s} + \widehat{\widetilde{d}}^{s}_{,j}\right) = {} & \left(G^{s}_{u}\right)^{\mathrm{T}}\Delta x_u + g^{s}_{u}\Delta\tau_u + d\widetilde{t}_{u,g} \\ & + \mu_j \widetilde{\iota}^{s}_{u} + \widetilde{d}_{u,j,g}\end{aligned} \tag{15}$$

where the subscript u denotes the user. G^{s}_{u} denotes the satellite-to-user unit direction vector, and Δx_u represents the user coordinate increment vector upon it’s a-priori values. The $\widehat{\widetilde{dt}}^{s}$, $\widehat{\widetilde{\delta}}^{s}_{,j}$ and $\widehat{\widetilde{d}}^{s}_{,j}$ with a hat above their modified forms stand for the estimates of the satellite clocks, satellite phase and code biases, respectively. The satellite code biases $\widehat{\widetilde{d}}^{s}_{,j}$ are only delivered to users when $j > 2$.

The estimable user receiver clock, the essential parameter to be considered in this study, is formulated as follows:

$$d\widetilde{t}_{u,g}(t_i) = dt_{1u}(t_i) + d_{1u,\mathrm{IF},g}(t_1) \tag{16}$$

where $dt_{1u}(t_i)$ denotes the epoch-wise clock difference between the user and the reference network station. $d_{1u,\mathrm{IF},g}(t_1)$ is the first-epoch IF code bias between the user and the reference network station, for constellation g. By adding time links for the hardware biases as mentioned before, the receiver clock has the opportunity to contain only one epoch of the receiver code bias instead of the time-varying all-epoch code biases. As such, the estimated receiver clock here is in this way analytically free from the time variation of the receiver code bias.

The frequency instability of $d\widetilde{t}_{u,g}(t_i)$ could be strongly influenced by the network products, which is to be discussed in Section 4. This influence can, however, be significantly reduced when forming the difference between two user stations u and v:

$$d\widetilde{t}_{uv,g}(t_i) = dt_{uv}(t_i) + d_{uv,\mathrm{IF},g}(t_1) \tag{17}$$

As such, the time transfer discussed in this study is performed between two PPP-RTK user stations.

Considering the $d\widetilde{t}_{uv,g}(t_i)$ of different constellations, a weighted mean of $d\widetilde{t}_{uv,g}(t_i)$, denoted as $d\widetilde{t}_{uv}(t_i)$, can be obtained with:

$$d\widetilde{t}_{uv}(t_i) = \sum_{g=1}^{n}\left(\alpha_g d\widetilde{t}_{uv,g}(t_i)\right) \tag{18}$$

where n represents the number of constellations. The weighting coefficients α_g fulfill the following condition:

$$\sum_{g=1}^{n}\alpha_g = 1 \tag{19}$$

The formulation of the weighting coefficient α_g is to be discussed later in Section 4.1 with the test results.

As the true clock difference dt_{uv} does not distinguish between different constellations, based on Eqs. (17) and (18) can also be reformulated as:

$$d\widetilde{t}_{uv}(t_i) = dt_{uv}(t_i) + \sum_{g=1}^{n}\left(\alpha_g d_{uv,\mathrm{IF},g}(t_1)\right) \tag{20}$$

In this way, the estimable receiver clock difference $d\widetilde{t}_{uv}(t_i)$ is expected to be the sum of the epoch-wise clock difference itself $dt_{uv}(t_i)$ and a constant code hardware bias.

Like the network processing, the float ambiguities can be resolved with the LAMBDA method. With the PAR enabled, the ASR threshold is set to 99.9 % on the user side. The threshold for the ratio test is set to three as in the network processing.

In (near-)real-time applications, the process above can be summarized as follows. The network processing center obtains the GNSS observations of network stations in real-time, calculates the network products, and broadcasts them to users. The users can then process their time differences to the reference network station. One of the users is suggested to be a timing lab. It transmits its time difference to other users, such that all other users can estimate their time difference with the timing lab. The processing, of course, takes time, but it is very limited compared to the traditional Integer Ambiguity Resolution (IAR)-enabled batch least-squares adjustment. The small latency can be bridged through short-term prediction if near-real-time products are insufficient for the corresponding application.

3. Measurement setup

In this study, a Continuously Operating Reference Stations (CORS) network located in Europe is used for the PPP-RTK time transfer (see Fig. 1). 15 network stations (shown in blue) form a network with the largest inter-station distance amounting to 1441 km. The station PTBB equipped with an H-Maser (the blue star) serves as the reference network station. Within the network, three user stations (the red stars) connected to H-Masers are used to assess the frequency instability of the PPP-RTK time transfer. The three stations form two long baselines BRUX-ONSA and WTZR-ONSA, with a length of 884 and 920 km, respectively. All the network and user stations are equipped with geodetic-grade receivers and antennas. Details of the two baselines are given in Table 1.

In this contribution, the PPP-RTK time transfer is performed using 30 s GPS observations on L1C, L2W and Galileo observations on E1C and E5Q from 1 to 7 May 2022. Four network stations do not track signals on the corresponding Galileo channels, and thus contribute only to the GPS processing. Within the seven test days, the histogram of the used GPS and Galileo satellite numbers above the elevation mask angle of 10 degrees is illustrated in Fig. 2. It can be observed that most of the time, 8 to 9 GPS satellites are available for processing, while the numbers of Galileo satellites are about 5 to 7.

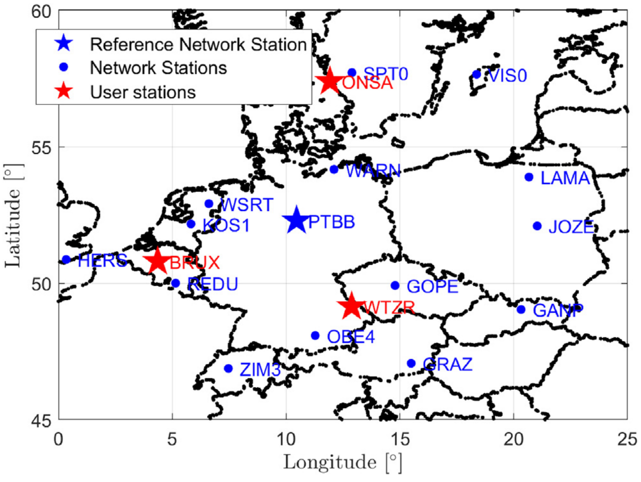

Fig. 1. Network and user stations used for the PPP-RTK time transfer.

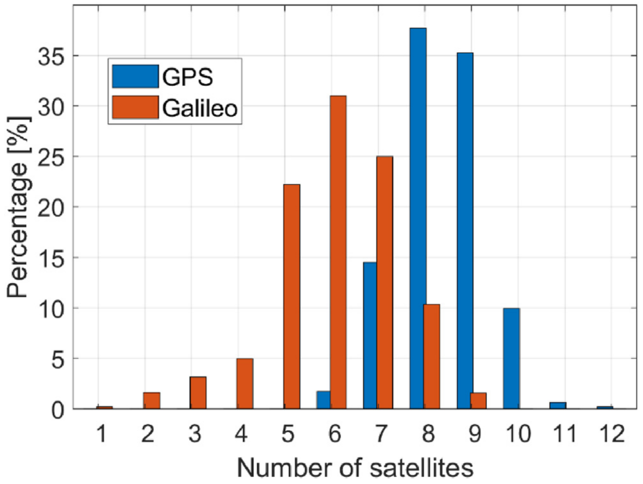

Fig. 2. Percentages of the visible satellite numbers (above the elevation mask angle of 10 degrees) for all test epochs, and all the network and user stations.

In the network processing, the coordinates of all network stations are fixed to their ground truths that were post-processed with the Bernese GNSS Software V5.2 (Dach et al. 2015) with daily batch least-squares adjustment. Final satellite clocks and orbits provided by the Center for Orbit Determination in Europe (CODE) (Dach et al. 2020) were used to process the ground-truth coordinates. For the PPP-RTK processing, the real-time GNSS satellite orbits produced by the National Centre for Space Studies (CNES) in France (Kazmierski et al. 2018) are used. No external satellite clocks were introduced in the processing.

4. Test results

In this section, the results of the real-time time transfer are discussed for the two long baselines as mentioned in the last section, i.e., the 884 km baseline BRUX-ONSA, and the 920 km baseline WTZR-ONSA. The analysis distinguishes between three user estimation modes:

- Fixed mode: The ground-truth user coordinates are introduced into the user processing as known values, i.e., Δx_u is not estimated in Eqs. (14) and (15);
- Static mode: The user coordinates increment vector Δx_u is estimated, but constrained as constant in time.

Table 1
Information on the two baselines used for the PPP-RTK time transfer.

Station	Baseline	Length (km)	Clock Type	Location	Receiver Type	Antenna Type
BRUX	BRUX-ONSA	884	External H-Maser	Brussels, Belgium	SEPT POLARX5TR	JAVRINGANT_DM SCIS
ONSA	WTZR-ONSA	920		Onsala, Sweden		AOAD/M_B OSOD
WTZR				Bad Koetzting, Germany	LEICA GR50	LEIAR25.R3 LEIT

- Kinematic mode: The user coordinates increment vector Δx_u is estimated independently at each epoch, without any temporal constraint.

The three estimation modes above are indexed with “FX”, “ST” and “KN”, respectively. As the user coordinates, especially the height component, are highly correlated with the receiver clocks, the user coordinate estimation mode influences both the convergence of the real-time time transfer and the frequency instability after convergence.

In addition to the different user coordinate estimation modes, the test results discussed in this section also distinguish between the PAR-enabled and the ambiguity-float solutions, for both the network and the users. Table 2 summarizes all the estimation modes regarding the user coordinate estimation and ambiguity resolution, with their indices given in the first column.

In the following sub-section, the time transfer results of the two long baselines (BRUX-ONSA and WTZR-ONSA) are first discussed before and after forming the between-receiver clock differences, and before and after combining the multi-constellation clocks. The discussions continue next with respect to their stabilities and the convergence times for all the solution types, as mentioned in Table 2.

Table 2
Indices for different user coordinate estimation modes and ambiguity resolution strategies.

Index	Network Ambiguity Resolution	User Ambiguity Resolution
Nf-Uf	Float	Float
Nf-Ux	Float	PAR-enabled
Nx-Uf	PAR-enabled	Float
Nx-Ux	PAR-enabled	PAR-enabled
	User Coordinate Estimation Mode	
FX	User coordinates fixed to known values	
ST	User coordinates estimated statically	
KN	User coordinates estimated kinematically	

4.1. Frequency instability of multi-constellation clocks

The network processing is performed continuously from 1 to 7 May 2022, while the user processing starts three hours later, after the network processing, to allow for its convergence. The first hour of the user processing was not used due to its convergence, which will be discussed in Section 4.3. Each user has 164 h of processing time that is used for the frequency instability analysis in this section.

As mentioned in Section 2.2, the estimated $d\tilde{t}_{u,g}(t_i)$ (Eq. (16)), denoted as $\widehat{d\tilde{t}}_{u,g}(t_i)$, contains the clock difference between the user and the network reference station in addition to the between-receiver IF code bias at the initial time t_1. Although the network reference station PTBB is also connected to an external H-Maser like the user stations, the calculated $\widehat{d\tilde{t}}_{u,g}(t_i)$ is affected by the network products and does not reflect the good frequency stability of the involved clocks. The influences, however, can be largely reduced by differencing $\widehat{d\tilde{t}}_{u,g}(t_i)$ with that of another user station, e.g. $\widehat{d\tilde{t}}_{v,g}(t_i)$, producing the time difference between the user baselines $\widehat{d\tilde{t}}_{uv,g}(t_i)$. This is illustrated in Fig. 3. In this figure, the 7-day GPS clock residuals of $\widehat{d\tilde{t}}_{u,\mathrm{G}}$ (Eq. (16)) and $\widehat{d\tilde{t}}_{uv,\mathrm{G}}$ (Eq. (17)) are shown in the left and right panel, respectively, after detrending with a quadratic polynomial. The subscript G stands for the GPS constellation. The first processing hour is not considered due to the solution convergence as mentioned before. Note that both the GPS and Galileo measurements are considered in the processing, but only the GPS clocks are shown in the figures. The ambiguity-float solutions are used at both the network and the user sides (the “Nf-Uf” option in Table 2), and the user static coordinates are estimated (the “ST“ option in Table 2). It can be seen that the common systematic effects are largely reduced by forming the between-receiver differences. The 7-day standard deviations (STDs) of the clock residuals amount to about 0.20 ns, 0.17 ns, and 0.18 ns for the three station pairs in the left panel of Fig. 3. They are reduced to 0.07 ns and 0.11 ns for the two station pairs in the right panel of Fig. 3 after the differencing, i.e., form-

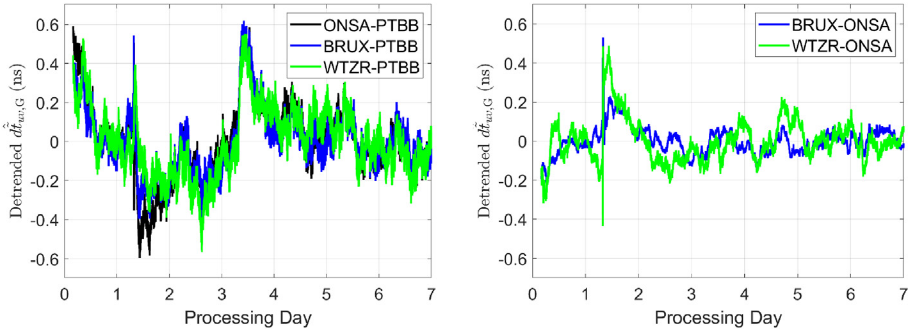

Fig. 3. The 7-day GPS clock residuals $\widehat{d\tilde{t}}_{u,\mathrm{G}}$ (Eq. (16)) (left) and $\widehat{d\tilde{t}}_{uv,\mathrm{G}}$ (Eq. (17)) (right) after detrending a quadratic polynomial. The “Nf-Uf” and the “ST” options (see Table 2) are used for the plots.

ing $d\widehat{\tilde{t}}_{uv,\mathrm{G}}$ using the $d\widehat{\tilde{t}}_{u,\mathrm{G}}$ and $d\widehat{\tilde{t}}_{v,\mathrm{G}}$.

It is noted that the 7-day STDs of the detrended clocks are larger than the daily STDs due to the remaining long-term systematic effects. The averaged 24 h STDs of the clock residuals for $d\widehat{\tilde{t}}_{uv,\mathrm{G}}$ amount to about 0.03 ns and 0.07 ns, respectively, for the baselines BRUX-ONSA and WTZR-ONSA. The 24 h clock residuals from 4:00 (GPST), 1 May 2022 to 4:00, 2 May 2022, are shown in Fig. 4 as a representative example.

The GPS clock $d\widehat{\tilde{t}}_{uv,\mathrm{G}}$ is not the only option when multi-constellation measurements are processed. As mentioned in Section 2.2, a GPS/Galileo-combined solution can be generated by giving the clocks of each constellation a proper weight. As true clocks (error-free clocks) do not vary with the constellation, only the first-epoch between-receiver IF code biases are constellation-specific and will be reformed. To determine the weighting factors, the coefficient α_g in Eq. (18) needs to be first determined to possibly reduce the Modified Allan Deviation (MDEV) (Allan and Barnes 1981) at a certain averaging time ($\tau0$). α_g is expected to minimize the following term:

$$\sigma^2_{\tau0,\mathrm{GE}} = \alpha^2_{\mathrm{G}}\sigma^2_{\tau0,\mathrm{G}} + \alpha^2_{\mathrm{E}}\sigma^2_{\tau0,\mathrm{E}} \rightarrow \min \tag{21}$$

where $\sigma_{\tau0,g}$ ($g = \mathrm{G}$, E) denotes the MDEV of $d\widehat{\tilde{t}}_{uv,g}(t_i)$ at an averaging time of $\tau0$, and $\sigma_{\tau0,\mathrm{GE}}$ denotes the corresponding MDEV of the combined clocks $d\widehat{\tilde{t}}_{uv}(t_i)$. The subscripts G and E stand for the GPS and Galileo constellation, respectively. Based on the condition that $\alpha_{\mathrm{G}} + \alpha_{\mathrm{E}} = 1$ (see Eq. (19)), and assuming that $k = \sigma^2_{\tau0,\mathrm{E}}/\sigma^2_{\tau0,\mathrm{G}}$, Eq. (21) can be reformulated as:

$$\begin{aligned}\sigma^2_{\tau0,\mathrm{GE}} &= \alpha^2_{\mathrm{G}}\sigma^2_{\tau0,\mathrm{G}} + \alpha^2_{\mathrm{E}}\sigma^2_{\tau0,\mathrm{E}} = \alpha^2_{\mathrm{G}}\sigma^2_{\tau0,\mathrm{G}} + (1-\alpha_{\mathrm{G}})^2 k\sigma^2_{\tau0,\mathrm{G}} \\ &= \left((k+1)\alpha^2_{\mathrm{G}} - 2k\alpha_{\mathrm{G}} + k\right)\sigma^2_{\tau0,\mathrm{G}}\end{aligned} \tag{22}$$

To minimize $\sigma^2_{\tau0,\mathrm{GE}}$, for $0 < \alpha_{\mathrm{G}} < 1$, α_{G} can be expressed as:

$$\alpha_{\mathrm{G}} = \frac{k}{k+1} \tag{23}$$

Correspondingly, the Galileo-specific coefficient α_{E} will equal to $1/(k+1)$. As such, in this study, the weighting coefficients are formed based on $\sigma_{\tau0,\mathrm{G}}$ and $\sigma_{\tau0,\mathrm{E}}$, instead of employing external knowledge of the GNSS signal properties.

Taking $\tau0 = 30$ s as an example, the 7-day single and multi-constellation clock residuals and their corresponding MDEVs are plotted in Fig. 5 for the 884 km baseline BRUX-ONSA with the “Nf-Uf” and the “ST” processing options (see Table 2). The MDEV at $\tau0 = 30$ s amounts to $2.8\ \times 10^{-13}$ and $2.1\ \times 10^{-13}$ for the GPS and Galileo clocks, respectively. The weighting factor α_g thus equals to about 0.43 and 0.57 for GPS and Galileo, respectively, based on Eq. (21–23). It can be seen that combining the single-constellation clocks has reduced the STD by around 0.01 to 0.02 ns. The combined MDEVs (see the green line in the right panel of Fig. 5) generally also approach the lower Galileo-only MDEVs (shown in blue) in short to mid-term, and the lower GPS-only MDEVs (black) after 10^4 s.

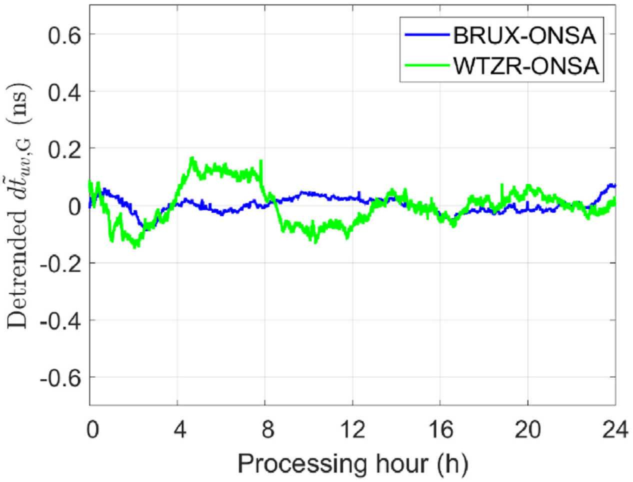

Fig. 4. The 24 h GPS clock residuals $d\widehat{\tilde{t}}_{uv,\mathrm{G}}$ (Eq. (17)) after detrending with a quadratic polynomial. The “Nf-Uf” and the “ST” options (see Table 2) are used for the plots.

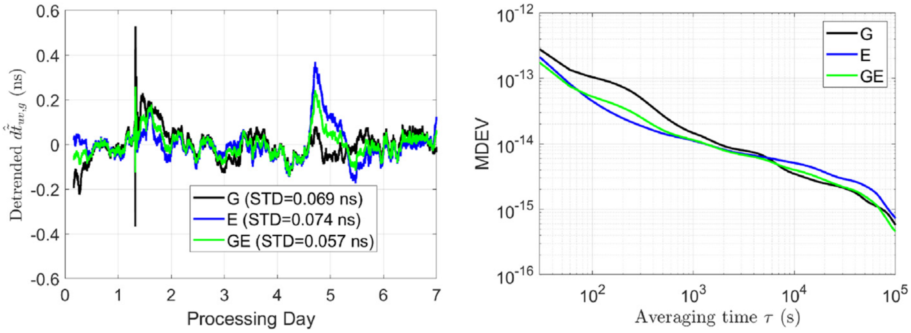

Fig. 5. The detrended 7-day residuals (left) and MDEVs (right) of the between-receiver clocks for baseline BRUX-ONSA in GPS (G), Galileo (E) and GPS/Galileo-combined (GE) cases. The “Nf-Uf” and the “ST” options (see Table 2) are used for the plots.

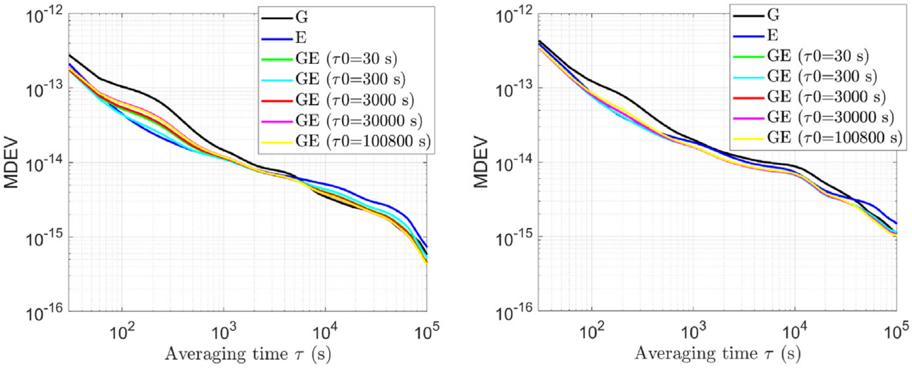

Fig. 6. MDEVs of the between-receiver clocks for the 884 km baseline BRUX-ONSA (left) and the 920 km baseline WTZR-ONSA (right) in GPS (G), Galileo (E) and GPS/Galileo-combined (GE) cases. The “Nf-Uf” and the “ST” options (see Table 2) are used for the plots.

Changing the averaging time $\tau 0$ would influence the combined MDEVs. Fig. 6 shows the MDEVs of differently combined clock differences ($\widehat{\widehat{dt}}_{uv}$) when determining the weighting coefficients by setting $\tau 0$ to different values. The green lines with $\tau 0 = 30$ s delivers an MDEV of 1.7×10^{-13} at an averaging time of 30 s for the 884 km baseline BRUX-ONSA, and an MDEV of 3.5×10^{-13} for the 920 km baseline WTZR-ONSA. The yellow lines with $\tau 0 = 100800$ s deliver an MDEV of 4.3×10^{-16} at an averaging time of 100800 s for BRUX-ONSA, and an MDEV of 1×10^{-15} for WTZR-ONSA. The combined MDEVs are not always lower than the single MDEVs, as the $\widehat{dt}_{uv,g}$ is not purely white phase noise, and are not uncorrelated between the two constellations. However, the combined MDEVs are near to or below the lower MDEV of the two at different averaging times. In general, a proper combination of multi-constellation clocks would deliver improved frequency stability.

The weighting coefficients and the 7-day STDs of the detrended between-receiver clocks are listed in Table 3 for the two investigated baselines. The combined STDs are reduced compared to the single-constellation cases, and do not vary much for different $\tau 0$. In general, they slowly reach their minimum values when $\tau 0$ is set to long averaging times, i.e., with an STD of about 0.056 ns for the 884 km baseline BRUX-ONSA and 0.089 ns for the 920 km baseline WTZR-ONSA, respectively. In the following contexts, the GPS/Galileo-combined clock difference $\widehat{\widehat{dt}}_{uv}$ with $\tau 0$ set to 100800 s are analyzed for the two baselines.

4.2. Frequency instability of the PPP-RTK time transfer

In the last sub-section, the “Nf-Uf” and the “ST” options (see Table 2) were used to demonstrate the benefits of combining the GPS with Galileo clocks. Other estimation modes with respect to the user coordinate estimation and the ambiguity resolution would lead to differences in the frequency instability.

The MDEVs of the $\widehat{\widehat{dt}}_{uv}$ under different estimation modes are illustrated in Fig. 7 for the two baselines. The ambiguity-float network products are used (the “Nf” option) for the plots, as using the PAR-enabled network products (the “Nx” option) delivers very similar results. The MDEVs and the selected averaging times are listed in Table 4 for the “Nf-Uf” option under the fixed, static and kinematic estimation modes. From Fig. 7 and Table 4 it can be observed that:

- When excluding the first hour due to the solution convergence, the frequency instability of the fixed mode (i.e., the “FX” option) is similar to that of the static mode (the “ST” option);

Table 3
Weighting coefficients and 7-day STDs of the detrended between-receiver clocks for the two test baselines in the GPS, Galileo and GPS/Galileo-combined cases. The values apply to the “Nf-Uf” and the “ST” options (see Table 2).

Constellation	$\tau 0$(s)	BRUX-ONSA (884 km)			WTZR-ONSA (920 km)		
		α_G	α_E	**STD (ns)**	α_G	α_E	**STD (ns)**
G	None	1	0	0.069	1	0	0.109
E		0	1	0.074	0	1	0.122
GE	30	0.43	0.57	0.057	0.47	0.52	0.090
	300	0.27	0.73	0.061	0.36	0.64	0.094
	3000	0.47	0.53	0.057	0.47	0.53	0.090
	30,000	0.58	0.42	0.056	0.47	0.53	0.090
	100,800	0.56	0.44	0.056	0.57	0.43	0.089

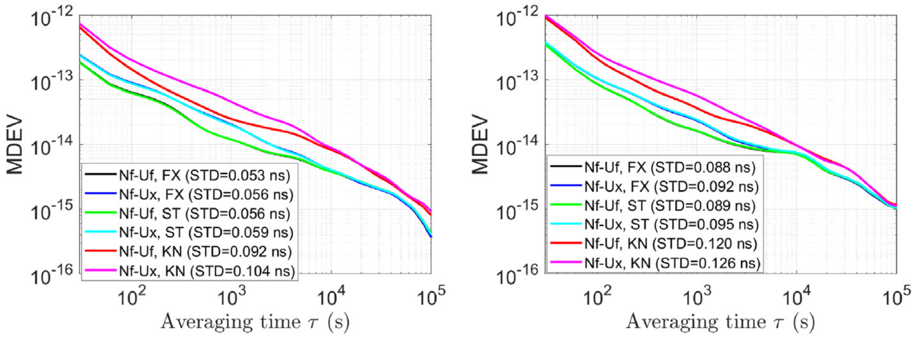

Fig. 7. MDEVs of the 884 km baseline BRUX-ONSA (left) and the 920 km baseline WTZR-ONSA (right) under different estimation modes.

Table 4
MDEVs of the between-receiver clocks for the baselines BRUX-ONSA and WTZR-ONSA under the "Nf-Uf" option for the fixed ("FX"), static ("ST") and kinematic ("KN") modes.

Averaging Time (s)	**BRUX-ONSA (884 km)**			**WTZR-ONSA (920 km)**		
	FX	**ST**	**KN**	**FX**	**ST**	**KN**
30	1.9×10^{-13}	1.8×10^{-13}	6.5×10^{-13}	3.5×10^{-13}	3.5×10^{-13}	9.2×10^{-13}
90	6.7×10^{-14}	6.5×10^{-14}	1.6×10^{-13}	9.4×10^{-14}	9.4×10^{-14}	2.4×10^{-13}
990 ($\sim 10^3$)	1.2×10^{-14}	1.2×10^{-14}	2.5×10^{-14}	1.6×10^{-14}	1.6×10^{-14}	3.7×10^{-14}
9900 ($\sim 10^4$)	3.8×10^{-15}	3.8×10^{-15}	8.3×10^{-15}	7.1×10^{-15}	7.1×10^{-15}	9.7×10^{-15}
100,800 ($\sim 10^5$)	3.7×10^{-16}	4.3×10^{-16}	8.0×10^{-16}	1.0×10^{-15}	1.0×10^{-15}	1.2×10^{-15}

- The kinematic mode (the "KN" option) delivers a worse frequency stability than the fixed and static modes, especially in the short term. This is caused by the high correlation between the receiver clock estimates and the kinematic height components;
- The PAR at the user processing did not improve the frequency stability in our tests, especially in short- to mid-term. This will be discussed later in this section;
- In general, the GPS and Galileo-combined clocks can reach an MDEV at the level of sub-10^{-15} to 10^{-15} at an averaging time of about 10^5 s in all the tested estimation modes, for both baselines, and in both the ambiguity-float and PAR-enabled cases. The kinematic mode generally delivers a worse short- to mid-term frequency stability compared to the fixed and static modes.

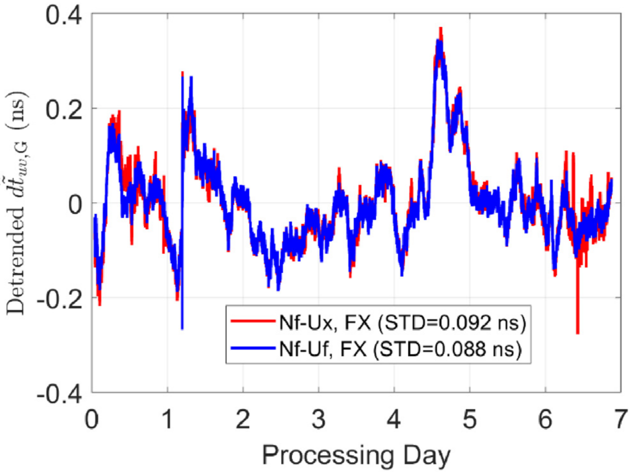

Fig. 8. Detrended clock residuals of $d\widehat{\tilde{t}}_{uv}$ in the static mode with the ambiguities remaining float (the "Uf" option) and with the PAR enabled. The baseline WTZR-ONSA is used for the plot.

Having a closer look at the ambiguity-float and PAR-enabled detrended clock residuals of $d\widehat{\tilde{t}}_{uv}$ in the static mode as an example (see Fig. 8), it can be observed that the PAR-enabled solutions are not advantageous in maintaining short- to mid-term frequency stability. The number of resolved ambiguities in PAR could vary from one epoch to the next, and possible wrong ambiguity resolution could lead to instabilities.

The 7-day STDs of the detrended clock residuals under different estimation modes are listed in Table 5. It can be seen that the STDs of the PAR-enabled solutions are similar to those of the float solutions, with slight degradations. In general, an STD of 0.05 ns to 0.1 ns can be expected for the static and fixed modes over 7 days, and the STDs in the kinematic mode are around 0.1 ns.

Table 5
7-day STDs of the detrended clock residuals after convergence under different estimation modes.

Estimation mode	**BRUX-ONSA (884 km)**		**WTZR-ONSA (920 km)**	
	Nf (ns)	**Nx (ns)**	**Nf (ns)**	**Nx (ns)**
Uf, FX	0.053	0.053	0.088	0.091
Ux, FX	0.056	0.055	0.092	0.096
Uf, ST	0.056	0.057	0.089	0.091
Ux, ST	0.059	0.059	0.095	0.096
Uf, KN	0.092	0.096	0.120	0.122
Ux, KN	0.104	0.103	0.126	0.129

4.3. Convergence time

For real-time time transfer, the solution convergence time to high precision is an issue to be concerned about, especially for kinematic users that might need to re-initialize the user processing frequently. In this section, the behaviors of the first-hour GPS/Galileo-combined clocks $\widehat{d\hat{t}}_{uv}$ are analyzed in detail. A quadratic polynomial is determined based on the $\widehat{d\hat{t}}_{uv}$ from the second to the 24-th hour after each processing start and used for the detrending. The polynomial is, in such a case, not influenced by the bad precision during the convergence. The first-hour $\widehat{d\hat{t}}_{uv}$ are then detrended with this polynomial. The starting time is shifted by 6 h in each round of the processing, delivering 24 samples of convergence lines based on the method mentioned above.

The left panel of Fig. 9 shows the median absolute clock residuals, i.e., the 50 % percentile lines, of the BRUX-ONSA baseline within the first processing hour under different estimation modes. It can be seen that the different estimation modes lead to differences in the solution convergence times. The fixed mode (“FX”) performs the best with almost instantaneous convergence to 0.5 ns, and only a few minutes to converge to 0.3 ns (shown as blue and black lines in the figure). The static mode (“ST”) performs better than the kinematic mode (“KN”). It takes not more than 4 min to converge to 0.3 ns in the static mode (green and cyan lines), while the corresponding convergence time is extended to about 10 min in the kinematic mode (red and magenta lines).

From the left panel of Fig. 9, it can be seen that the PAR-enabled clocks (“Ux”) do not show quicker convergence than the ambiguity-float clocks (“Uf”). This is possibly caused by the relatively low fix rate, as shown in the right panel of Fig. 9. The fix rate is calculated by dividing the number of the fixed de-correlated ambiguities by the total number of the de-correlated ambiguities using the LAMBDA method. With the threshold for the ratio test set to three as mentioned before, the fix rate in the right panel of Fig. 9 is shown to be around 20 % to 30 %. Setting lower thresholds in the ratio test. Not using the ratio test would deliver a higher fix rate in the PAR, but could result in more wrongly fixed ambiguities as well. Compared with the user coordinates processing mode, the wrongly fixed ambiguities and the changing number of the fixed ambiguities between subsequent epochs could more significantly disturb the frequency stability of their highly correlated clock parameters. As the frequency stability of the estimated between-station clocks matters more than the clock accuracies in the MDEVs, based on the results in this contribution, the ambiguity-float solutions could be a “safer” solution for the filter-based long-baseline time transfer in real time.

The median convergence times to 1 ns, 0.5 ns and 0.3 ns are given in Table 6 for both baselines. The estimation mode becomes a determining factor for the convergence time. In general, for all estimation modes and both baselines, the clock residuals can converge to 1 ns within 2 min. The clock residuals in the fixed mode can converge to 0.3 ns within a few minutes, while in the kinematic mode the convergence time is around 10 to 15 min.

4.3.1. Convergence time with the LEO-augmentation

As mentioned in the introduction, the rapid geometry change brought by the LEO satellites is beneficial to accelerating the convergence time of the PPP-RTK time transfer. In this sub-section, using the planned configuration of the navigation-oriented LEO satellite constellation CentiSpace, the convergence of the time transfer is ana-

Table 6
Median convergence times of the clock residuals for the 884 km baseline BRUX-ONSA and the 920 km baseline WTZR-ONSA to 1 ns, 0.5 ns and 0.3 ns. The estimation modes in the first column are described in Table 2.

Estimation mode	**884 km BRUX – ONSA (min)**			**920 km WTZR – ONSA (min)**		
	1 ns	**0.5 ns**	**0.3 ns**	**1 ns**	**0.5 ns**	**0.3 ns**
Nf-Uf, FX	0.5	1.0	1.0	0.5	1.0	3.5
Nf-Ux, FX	0.5	0.5	2.0	0.5	1.0	3.0
Nf-Uf, ST	1.5	2.5	4.0	2.0	5.5	10.0
Nf-Ux, ST	1.5	2.5	3.5	2.0	5.5	14.5
Nf-Uf, KN	1.5	2.5	11.5	2.0	11.0	15.0
Nf-Ux, KN	1.5	2.5	9.5	2.0	11.0	15.0

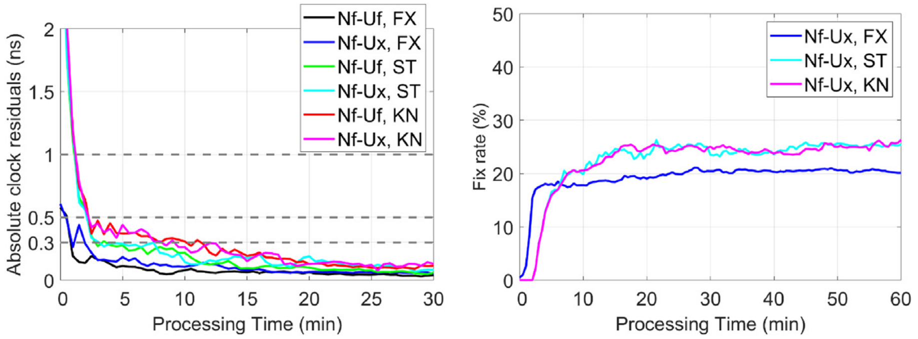

Fig. 9. The median absolute clock residuals of $\widehat{d\hat{t}}_{uv}$ after the detrending for the baseline BRUX-ONSA (left), and the average ambiguity fixing rate under different estimation modes (right).

Table 7
Orbital characteristics of the LEO satellite constellation CentiSpace.

Layer	Number	Orbital Plan	Orbital height (km)	Inclination (°)
A	120	12	975	55
B	30	3	1100	87.4

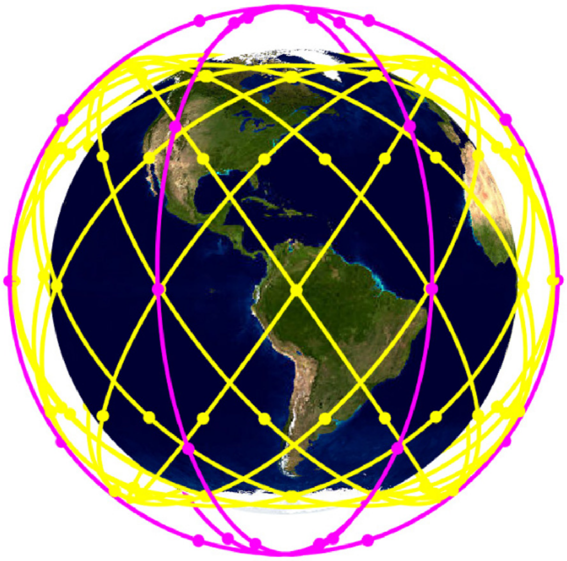

Fig. 10. The satellite configuration of the CentiSpace constellation. The yellow and magenta trajectories correspond to Layers A and B in Table 7, respectively.

lyzed for the two baselines under the fixed, the static and the kinematic modes.

The CentiSpace constellation has registered in the International Telecommunication Union (ITU) two layers of LEO satellites, as given in Table 7 (ITU 2022; Wang et al. 2022a). GNSS-interoperable signals are planned to be transmitted on the L1 and L5 frequencies. All satellites are assumed to have circular orbits, i.e., with an eccentricity of zero. The configuration of CentiSpace is illustrated in Fig. 10.

Based on the LEO satellite geometry described above, and since the constellation is under development, the O−C terms of the LEO satellites are simulated considering the following errors:

- ***Orbital errors*** The real-time orbital errors at sub-dm to dm-level. Based on the behaviors of the 30 min orbital prediction errors of the 800 km LEO satellite Sentinel-3B (Wang et al. 2022b), sinusoidal waves are simulated in the radial, along-track and cross-track directions for the LEO satellites in this study with an RMSE of 2.3 cm, 6.9 cm and 2.1 cm, respectively. A random phase shift is set in the sinusoidal waves for each satellite in each direction to distinguish the orbital errors of different satellites.
- ***The wet tropospheric delays*** The ZTDs are estimated in the PPP-RTK network processing using the GPS/Galileo real data for all the involved stations. The ZTDs obtained after one hour of convergence are mapped into the LOS direction with the Ifadis mapping function and used in the simulations.

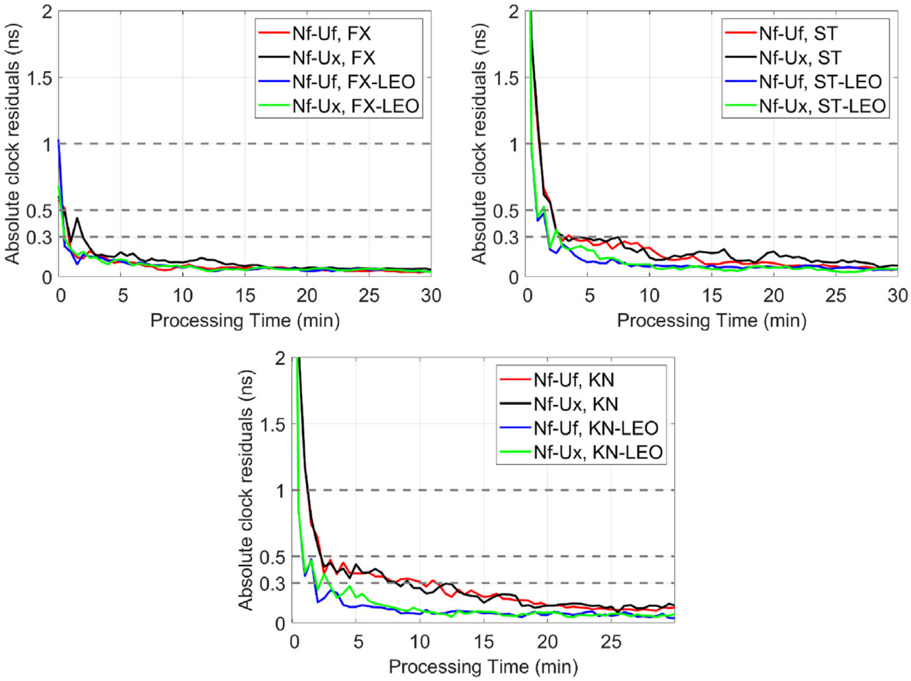

Fig. 11. Median convergence times of the absolute clock residuals without and with the LEO-augmentation of GNSS observations for the baseline BRUX-ONSA in (top left) the fixed mode, (top right) the static mode, and (bottom) the kinematic mode.

Table 8
Median convergence times of the absolute clock residuals without and with the LEO-augmentation of GNSS, separated by the sign "/". The estimation modes in the first column are described in Table 2.

Estimation mode	**884 km BRUX – ONSA (min)**			**920 km WTZR – ONSA (min)**		
	1 ns	**0.5 ns**	**0.3 ns**	**1 ns**	**0.5 ns**	**0.3 ns**
Nf-Uf, FX	0.5/0.5	1.0/0.5	1.0/0.5	0.5/0.5	1.0/0.5	3.5/0.5
Nf-Ux, FX	0.5/0.5	0.5/0.5	2.0/0.5	0.5/0.5	1.0/0.5	3.0/0.5
Nf-Uf, ST	1.5/0.5	2.5/1.0	4.0/2.0	2.0/0.5	5.5/1.0	10.0/3.0
Nf-Ux, ST	1.5/0.5	2.5/2.0	3.5/3.0	2.0/0.5	5.5/1.0	14.5/3.5
Nf-Uf, KN	1.5/0.5	2.5/1.0	11.5/2.0	2.0/0.5	11.0/1.5	15.0/2.5
Nf-Ux, KN	1.5/0.5	2.5/1.0	9.5/3.0	2.0/0.5	11.0/1.5	15.0/3.5

- ***The hardware biases*** The satellite phase and code hardware biases are simulated for each satellite separately as random-walk processes with a spectral density parameter of 0.0001 $m/\sqrt{s}$. Correspondingly, the receiver phase and code biases are simulated with a spectral density parameter of 0.001 $m/\sqrt{s}$.
- ***The noise*** The phase and code noise are simulated with a zenith-referenced standard deviation of 0.002 m/s and 0.2 m/s and the elevation-dependent weighting function $\sin^2(\theta_e)$.

The satellite/receiver clock errors and the ionospheric delays are independently estimated for LEO satellites without applying any temporal models. Their values are thus not of concern and set to zeros in the simulations. Note that the LEO receiver clocks are estimated but not used to combine the multi-constellation between-receiver clock $\widehat{d\tilde{t}}_{uv}$ (Eq. (18)). The elevation mask angle for LEO satellites is lowered to 5 degrees, as the LEO satellite signals are expected to have nearly whitened multipath due to the faster satellite speed and the capability to better penetrate obstacles due to their stronger signal strength.

Fig. 11 shows the median convergence times of the absolute clock residuals when detrending the 24 h clocks as explained in Section 4.3, without and with LEO-augmentation. It can be observed that the LEO-augmentation of GNSS (GPS + Galileo) satellites has shortened the convergence times, especially in the kinematic mode (bottom panel). The convergence times with and without the LEO-augmentation are also listed in Table 8. With the LEO-augmentation, the clock residuals can converge to 1 ns within 30 s, i.e., in one epoch, for all the three estimation modes; and the convergence time to 0.3 ns is within 3.5 min for all estimation modes. For the fixed mode, it takes only one epoch (30 s) to converge to 0.3 ns. In contrast to the significant differences between the convergence times in the kinematic and static/fixed modes without the LEO-augmentation, adding the LEO satellites makes the convergence time similar in all the estimation modes. In other words, the convergence time with the LEO-augmentation is less sensitive to the original estimation modes.

5. Conclusions

High-precision time transfer has been discussed for decades using various methods. Frequency instability at the sub-10^{-16} level can be achieved over one week when using the IPPP method, provided that high-precision final orbital and clock corrections can be input in the post-processed batch least-squares adjustment. For real-time time transfer, short-baseline users can also rely on the RTK time transfer. It relieves the high requirements of the external high-precision orbits and clocks, but has limits on the time transfer performance when the baseline length exceeds a certain threshold, e.g., hundreds of kilometers.

PPP-RTK combines the advantages of PPP and RTK. The advantages have positively influenced the real-time positioning over tens of years. Similarly, it can exhibit advantages in the real-time time transfer. In this study, using a thousand-kilometer-scale network in Europe, the PPP-RTK method is tested for real-time long-baseline time transfer. By delivering the satellite clocks and phase biases produced by a regional network, the users separated by nearly a thousand kilometers away can estimate their receiver clocks. The time transfer, in the end, is realized through differencing of the estimable clock parameters between two PPP-RTK users.

Using dual-frequency GPS and Galileo signals, the time transfer is tested for the 884 km baseline BRUX-ONSA, and the 920 km baseline WTZR-ONSA based on a real-time filter. An algorithm was introduced to combine the multi-constellation clock estimates to achieve better frequency stability. The estimation is performed in the station fixed, static and kinematic processing modes. The results showed that in the fixed and static modes, the MDEV at an averaging time of about 10^5 s can reach the level of sub-10^{-15} to 10^{-15}. Under the kinematic mode, the MDEV is worse in the short term, but can also reach around 10^{-15} at an averaging time of about 10^5 s. The convergence times show a strong dependence on the estimation modes, with the fixed mode behaving the best, the static mode the second best, and the kinematic mode the worst. For the GPS and Galileo combined clocks, it takes not more than 2 min to converge to 1 ns, and not more than 15 min to converge to 0.3 ns in all the three estimation modes. An extension analysis for the convergence time was performed when adding the 150 LEO satellites based on the CentiSpace configuration. The LEO-augmentation is found to be able to accelerate the convergence of the GNSS-based between-station clock residuals, especially in the kinematic mode. In such a case, the clock residuals can converge to 1 ns and 0.3 ns within 30 s and 3.5 min, respectively, for all the three estimation modes.

For applications of the proposed method in real life, some challenges still exist. The UDUC PPP-RTK model requires a consistent understanding of the parametrization at the user side similar to those applied at the network side, which is different from the traditional IF combination. To enable a (near-)real-time time transfer, internet-based data transmission is required at multiple steps, including transmission of the GNSS measurements of the network stations to a data processing center, transmission of the network products to users, and transmission of the clock differences from one user to other users. As a prerequisite for good results in the proposed time-transfer method, it is essential to guarantee complete and continuous data transmission.

Declaration of Competing Interest

The authors declare that they have no known competing financial interests or personal relationships that could have appeared to influence the work reported in this paper.

Acknowledgments

This research is funded by the National Time Service Center, Chinese Academy of Sciences (CAS) (No. E167SC14), the National Natural Science Foundation of China (No. 12073034), and the Australian Research Council Discovery Project (No. DP 190102444). We acknowledge also the support of the international GNSS monitoring and assessment system (iGMAS) at the National Time Service Center, and the National Space Science Data Center, National Science & Technology Infrastructure of China (http://www.nssdc.ac.cn).

References

Allan, D.W., Barnes, J.A. 1981. A Modified “Allan Variance” with Increased Oscillator Characterization Ability. In Proc. 35th Ann. Freq. Control Symposium, USAERADCOM. 27-29 May 1981, Ft. Monmouth, NJ, USA, pp. 470-475.

Baarda, W. 1981. S-transformations and criterion matrices. Second revised edn. In Publications on Geodesy (New Series), Vol. 5, Nr. 1. Netherlands Geodetic Commission, Delft, The Netherlands, pp. 1-168.

Dach, R., Lutz, S., Walser, P., Fridez, P. 2015. Bernese GNSS Software Version 5.2. User manual, Astronomical Institute, University of Bern, Bern Open Publishing. doi: 10.7892/boris.72297.

Dach, R., Schaer, S., Arnold, D., Kalarus, M.S., Prange, L., Stebler, P., Villiger, A., Jäggi, A. 2020. CODE final product series for the IGS. Published by Astronomical Institute, University of Bern. doi: 10.7892/boris.75876.4

Feng, Y., Li, B. 2010. Four Dimensional Real Time Kinematic State Estimation and Analysis of Relative Clock Solutions. In Proc. of the 23rd International Technical Meeting of the Satellite Division of The Institute of Navigation (ION GNSS 2010), 21-24 September 2010, Portland, OR, USA, pp. 2092-2099.

Ifadis, I.I., 1986. The atmospheric delay of radio waves: modeling the elevation dependence on a global scale. Chalmers University of Technology, Göteborg, Sweden, Technical Report 38L,.

ITU, 2022. List of Space Networks/Earth Stations (By Frequency and Orbital Position). International Telecommunication Union. Accessed on January 25, 2022 at https://www.itu.int/snl/freqtab_snl.html.

Kazmierski, K., So nica, K., Hadas, T. 2018. Quality assessment of multi-GNSS orbits and clocks for real-time precise point positioning. GPS Solut., 22, 11. doi: 10.1007/s10291-017-0678-6.

Leick, A., 2004. GPS satellite surveying, Third edition. John Wiley and Sons, New York, p. 2004.

Li, B., Ge, H., Ge, M., Nei, L., Shen, Y., Schuh, H., 2019. LEO enhanced Global Navigation Satellite System (LeGNSS) for real-time precise positioning services. Adv. Space Res. 63 (1), 73–93. https://doi.org/10.1016/j.asr.2018.08.017.

Lyu, D., Zeng, F., Ouyang, X. 2019. Real-Time PPP Time Transfer With Ambiguity Resolution. 2019 IEEE 4th Advanced Information Technology, Electronic and Automation Control Conference (IAEAC), 20-22 December 2019, Chengdu, China. doi: 10.1109/IAEAC47372.2019.8997731.

Nardo, A., Li, B., Teunissen, P.J.G., 2016. Partial Ambiguity Resolution for Ground and Space-Based Applications in a GPS + Galileo scenario: A simulation study. Adv. Space Res. 57 (1), 30–45. https://doi.org/10.1016/j.asr.2015.09.002.

Noll, C.E., 2010. The Crustal Dynamics Data Information System: A resource to support scientific analysis using space geodesy. Adv. Space Res. 45 (12), 1421–1440. https://doi.org/10.1016/j.asr.2010.01.018.

Odijk, D., Zhang, B., Khodabandeh, A., Odolinski, R., Teunissen, P.J.G., 2015. On the estimability of parameters in undifferenced, uncombined GNSS network and PPPRTK user models by means of S-system theory. J. Geod. 90 (1), 15–44. https://doi.org/10.1007/s00190-015-0854-9.

Petit, G., 2021. Sub-10-16 accuracy GNSS frequency transfer with IPPP. GPS Solut. 25, 22. https://doi.org/10.1007/s10291-020-01062-2.

Petit, G., Leute, J., Loyer, S., Perosanz, F. 2017. Sub frequency transfer with IPPP: Recent results. In Proceedings of 2017 EFTF/IFCS, Besancon, France, 09-13 July 2017, pp. 784-787. doi: 10.1109/FCS.2017.8089035.

Petit, G., Kanj, A., Loyer, S., Delporte, J., Mercier, F., Perosanz, F., 2015. 1×10-16 frequency transfer by GPS PPP with integer ambiguity resolution. Metrologia 52, 301–309. https://doi.org/10.1088/0026-1394/52/2/301.

Qin, W., Su, H., Wei, P., Yang, H., Li, X., Yang, X., 2021. The analysis on BDS-3 carrier phase time transfer under the mode of basic navigation mode. Meas. Sci. Technol. 32 (12). https://doi.org/10.1088/1361-6501/ac17cd 125002.

Reid, T.G.R., Neish, A.M., Walter, T., Enge, P.K., 2018. Broadband LEO constellations for navigation. Navigation, Journal of the Institute of Navigation 65 (2), 205–220. https://doi.org/10.1002/navi.234.

Sun, B., Han, R., Liu, J., Zhang, Z., Wang, G., Chen, L., Liu, Y., Yang, X., 2021. A Multi-Region Real-Time Kinematic Time Service System Based on Beidou-3. Navigation Position & Timing 8 (4), 45–52. https://doi.org/10.19306/j.cnki.2095-8110.2021.04.006.

Teunissen, P.J.G., 1985. Zero order design: generalized inverses, adjustment, the datum problem and S-transformations. In: Optimization and Design of Geodetic Networks. Springer-Verlag, Berlin, Heidelberg, pp. 11–55.

Teunissen, P.J.G. 1993. Least-Squares Estimation of the Integer GPS Ambiguities. Invited lecture, Section IV Theory and Methodology, IAG General Meeting, Beijing, China, August 1993.

Teunissen, P.J.G., 1995. The least-squares ambiguity decorrelation adjustment: a method for fast GPS integer ambiguity estimation. J. Geod. 70 (1–2), 65–82. https://doi.org/10.1007/BF00863419.

Teunissen, P.J.G. and Verhagen, S. 2004. On the foundation of the popular ratio test for GNSS ambiguity resolution. In Proc. ION GNSS 2004, Long Beach, CA, September 2004; pp. 2529–2540.

Teunissen, P.J.G., Odijk, D., Zhang, B., 2010. PPP-RTK: results of CORS network-based PPP with integer ambiguity resolution. J. Aeronaut. Astronaut. Aviat., Ser. A 42 (4), 223–230.

Tu, R., Zhang, P., Zhang, R., Fan, L., Han, J., Hong, J., Liu, J., Lu, X., 2021. Real-time and dynamic time transfer method based on double-differenced real-time kinematic mode. IET Radar Sonar Navig. 15 (2), 143–153. https://doi.org/10.1049/rsn2.12027.

Wang, K., El-Mowafy, A., Qin, W., Yang, X., 2021. Integrity Monitoring of PPP-RTK Positioning; Part I: GNSS-based IM Procedure. Remote Sens. 14 (1), 44. https://doi.org/10.3390/rs14010044.

Wang, K., El-Mowafy, A., Wang, W., Yang, L., Yang, X., 2022a. Integrity Monitoring of PPP-RTK Positioning. Part II: LEO Augmentation. Remote Sens. 14 (7), 1599. https://doi.org/10.3390/rs14071599.

Wang, K., El-Mowafy, A., Yang, X., 2022b. URE and URA for predicted LEO satellite orbits at different altitudes. Adv. Space Res. 70 (8), 2412–2423. https://doi.org/10.1016/j.asr.2022.08.039.

Wübbena, G., Schmitz, M., Bagge, A. 2005. PPP-RTK: precise point positioning using state-space representation in RTK networks. In: Proc. ION GNSS 2005, Long Beach, CA, September 2005, pp. 2584–2594.

Xue, X., Qin, H., Lu, H., 2021. High-precision time synchronization of kinematic navigation system using GNSS RTK differential carrier phase time transfer. Measurement 176. https://doi.org/10.1016/j.measurement.2021.109132 109132.

Yang, L. 2019. The Centispace-1: A LEO Satellite-Based Augmentation System. In: The 14th Meeting of the International Committee on Global Navigation Satellite Systems. Bengaluru, India, 8 - 13 December 2019.